applied sciences

MDPI

Article

Compact Multibeam Near-Infrared Illuminator Based on a Center-Weighted Silica Waveguide Splitter

Hong-Shik Lee [1] and Sang-Shin Lee [2,*]

[1] KIEL Institute, Iksan-si 54630, Republic of Korea; back1454@gmail.com
[2] Department of Electronic Engineering, Kwangwoon University, Seoul 01897, Republic of Korea
* Correspondence: slee@kw.ac.kr; Tel.: +82-2-940-5581

Abstract

Compact illumination of multiple fixed regions requires coordinated control of the source distribution and free-space beam directions. This study presents a passive multibeam illuminator operating at $\lambda = 905$ nm that integrates a cascaded 1×5 silica waveguide splitter, a fiber-coupled laser diode, and an aspheric collimating lens. Beam propagation method calculations were used to examine field redistribution within the splitter, and the fabricated device was characterized through near-field and free-space measurements. The splitter provides five outputs with a nominal pitch of 30 μm and a dominant central intensity peak. A common lens converts this output array into an axial beam and two pairs of fixed off-axis beams within an approximately 4.5 cm module. The measured adjacent-beam spacings were 11.0, 21.16, and 29.94 mm at propagation distances of 3, 6, and 8 m, respectively, consistent with the distance-dependent separation expected from the output pitch and lens focal length. The central-beam diameter increased from 1.68 mm at 1 m to 6.85 mm at 8 m, corresponding to an effective full-angle spreading of approximately 0.042°. These results establish a compact guided-wave-to-free-space configuration for generating spatially separated near-infrared illumination beams without active steering.

Keywords: near-infrared illumination; silica waveguide splitter; planar lightwave circuit; cascaded Y-branch; multibeam illumination; beam collimation

1. Introduction

The spatial distribution of transmitted light is an important design parameter in active optical sensing. In time-of-flight cameras and light detection and ranging (LiDAR) systems, the illumination geometry must be considered together with the receiver configuration and the observation region [1,2]. Recent reviews describe integrated and nanophotonic approaches to compact beam generation and control [3,4]. For systems that monitor a central region and several adjacent regions, discrete beams can concentrate illumination in selected regions. A source array with a higher central peak intensity and lower lateral peak intensities provides a center-weighted intensity distribution. However, the output-facet intensity distribution alone does not determine the beam profiles at the observation plane. The beam directions, diameters, and center-to-center spacings also depend on the beam-forming optics and free-space propagation. These characteristics must therefore be evaluated together when designing a compact multibeam illuminator.

Several approaches have been developed to control illumination geometry and intensity distribution. Lutz and Poyet investigated laser-diode-stack beam shaping for compact long-range illumination [5], while Han et al. combined a waveguide-based homogeniza-

Check for updates

Academic Editor: Alessandro Lo Schiavo

Received: 29 October 2026
Revised: 17 November 2026
Accepted: 24 November 2026
Published: 26 November 2026

Copyright: © 2026 by the authors. Licensee MDPI, Basel, Switzerland. This article is an open access article distributed under the terms and conditions of the Creative Commons Attribution (CC BY) license.

tion structure with collimating optics to shape an infrared illumination field [6]. Compact source and beam-forming assemblies have been demonstrated using a 3D-printed freeform collimator for vertical-cavity surface-emitting laser (VCSEL) depth sensing [7], a miniature structured-light source [8], and a metasurface coupled to a photonic crystal surface-emitting laser (PCSEL) for infrared dot projection [9]. Freeform optical design provides additional control over illumination distributions [10]. Metasurfaces control optical wavefronts through spatially varying optical responses [11] and have been used for high-density structured-light projection in three-dimensional imaging [12] and multiport beam splitting with prescribed power ratios and output distributions [13]. A meta-fiber platform combining a Dammann grating with a collimating lens has also been investigated theoretically [14]. Another approach uses a lens to convert the positions of spatially separated emitters into different beam directions. This position-to-angle conversion has been demonstrated in scan-less sensing using wavelength-division demultiplexing [15], silica-based integrated beam steering for free-space optical frequency transfer [16], and a silicon photonic focal plane switch array for LiDAR [17]. These studies demonstrate different optical configurations for generating and directing multiple beams.

Integrated splitters distribute input light among multiple output waveguides. Compact silicon Y-junctions [18], multimode tapered branches [19], and broadband adiabatic transitions [20] have been investigated to improve splitter performance. Arbitrary power division has been demonstrated using shortcuts to adiabaticity [21] and digitally structured photonic devices [22]. Multichannel designs extend arbitrary-ratio splitting to integrated multimode photonics [23], with experimental demonstrations for both single- and multimode operation [24]. Recent studies have also reported a polarization-insensitive silicon nitride splitter with a fabricated 1 × 5 prototype providing uniform power distribution [25] and shape-optimized multiport splitters with nonuniform ratios [26]. Silica planar lightwave circuit (PLC) splitters include asymmetric three-waveguide structures for variable-ratio splitting [27], fabricated asymmetric 1 × 5 devices [28], and optimized nonuniform 1 × 5 devices [29]. Silica waveguide lenses have also been proposed for collimation in free-space optical cross connects [30]. These components provide methods for distributing guided light and forming free-space beams. When a splitter and a common lens are integrated into a fixed multibeam illuminator, the output intensity distribution, beam-axis separation, and beam expansion must be evaluated together to determine whether the illumination zones remain spatially separated over the intended propagation range.

In this study, we propose and implement a passive multibeam near-infrared (NIR) illuminator that integrates a cascaded 1 × 5 silica waveguide splitter, a fiber-coupled laser diode, and an aspheric collimating lens within an approximately 4.5 cm module. The five parallel outputs have a nominal pitch of 30 μm and form a source array with a dominant central intensity peak. The common lens converts these source positions into an axial beam and two pairs of fixed off-axis beams without active steering. Beam propagation method (BPM) calculations and near-field measurements characterize field redistribution and the output-facet intensity distribution. Free-space measurements over 1–8 m evaluate the beam patterns, adjacent-beam spacings, and central-beam expansion. This study experimentally demonstrates the conversion of a center-weighted silica output array into five fixed illumination beams and quantifies their separation and the expansion of the central beam over the measurement range. The resulting module provides a compact optical configuration for illuminating a central region and four adjacent regions along fixed directions.

2. Device Design and Fabrication

The illuminator employs a cascaded 1 × 5 silica waveguide splitter comprising a straight central waveguide and symmetrically arranged lateral branches, as shown in Figure 1. The

five parallel output waveguides form a linear source array with a nominal center-to-center pitch of 30 μm. Their transverse positions are −60, −30, 0, 30, and 60 μm relative to the central channel, corresponding to the outer, inner, central, inner, and outer outputs, respectively. Each waveguide has a square core cross section of 5 μm × 5 μm. The nominal core and cladding refractive indices at $\lambda = 905$ nm are 1.459 and 1.4532, respectively, corresponding to a relative refractive-index contrast of approximately 0.4%. The combined thickness of the upper and lower cladding layers is 40 μm. The device comprises a 1 mm input straight section, an 8 mm branching section with a nominal branch angle of 0.43°, and a 1 mm output straight section, giving a total length of 10 mm. The branching network redistributes the guided field among the output channels, while the parallel output section establishes the source positions presented to the collimating lens. The specified core dimensions describe the material geometry; the transverse optical-field distribution additionally depends on confinement and excitation and is not prescribed directly by the core width.

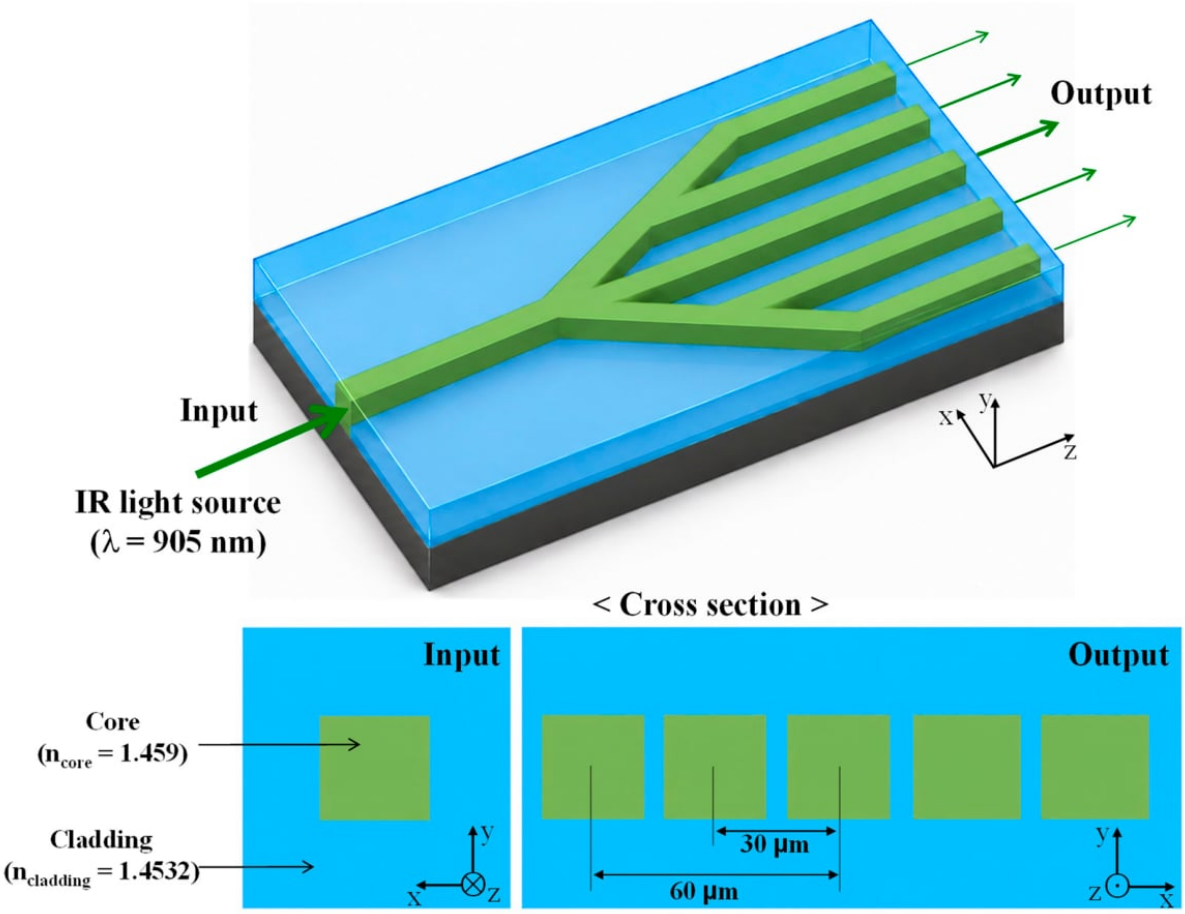

Figure 1. Layout and cross-sectional configuration of the cascaded 1 × 5 silica waveguide splitter. The nominal core dimensions are 5 μm × 5 μm, the adjacent output-channel pitch is 30 μm, and the core and cladding refractive indices are 1.459 and 1.4532, respectively.

Guided-field evolution through the complete branching structure was calculated using the beam propagation method (BPM) implemented in RSoft BeamPROP. The model incorporates the nominal geometry and refractive-index distribution specified above to evaluate field redistribution through the cascaded branches and the resulting relative intensity distribution at the five outputs. Figure 2a presents the calculated internal intensity distribution, and Figure 2b shows the corresponding transverse intensity profiles at successive propagation positions. These results describe the evolution from a single input region to five

spatially separated output regions. Because the field entering each downstream branching region has already undergone redistribution upstream, the final output must be interpreted as the response of the complete cascaded structure. It cannot be inferred by assigning ideal equal-power division independently to each junction. The internal intensity map identifies the propagation paths, while the transverse profiles show the relative excitation of the central and lateral regions along the device.

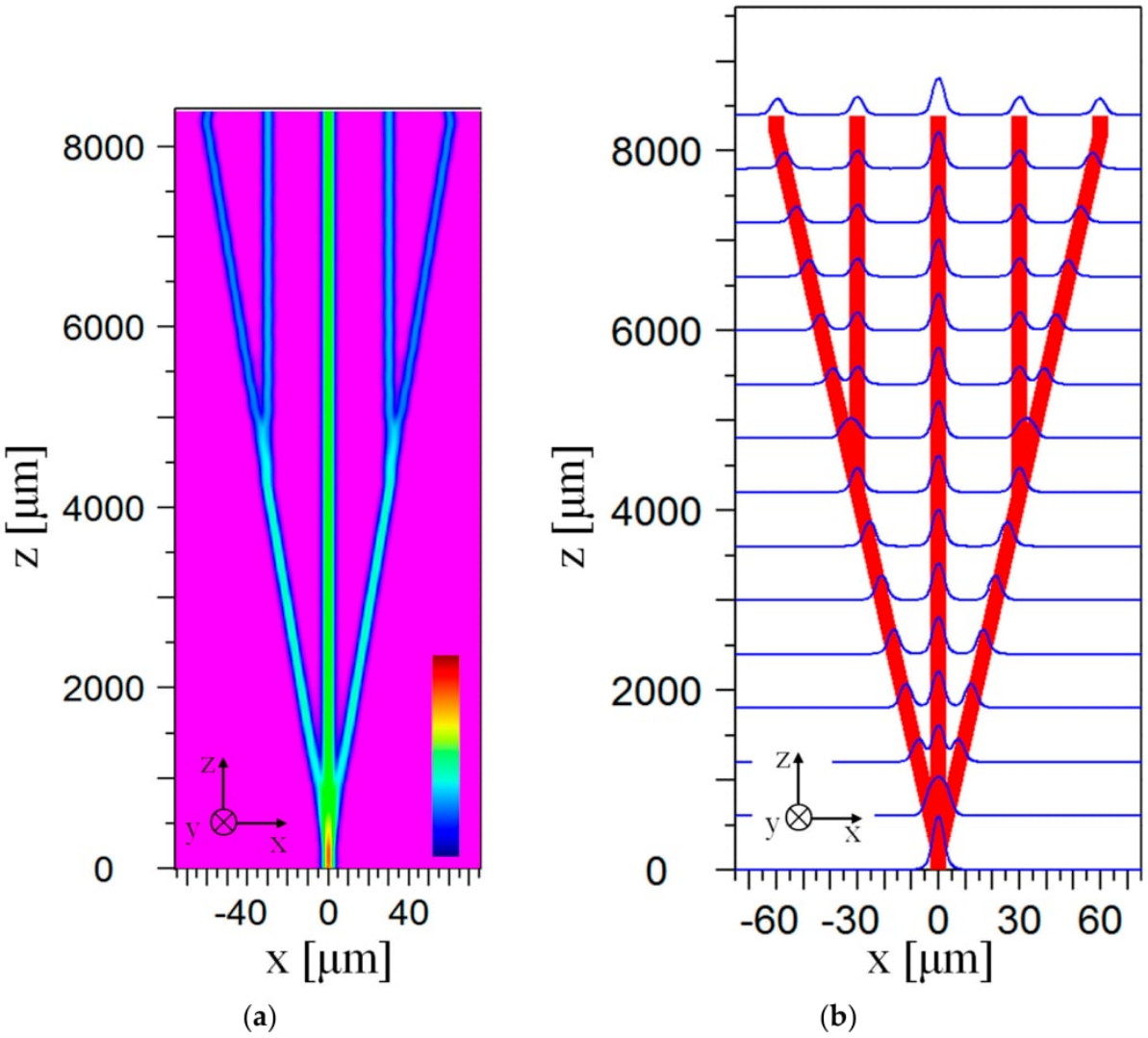

Figure 2. BPM analysis of the cascaded silica waveguide splitter: (**a**) calculated internal intensity distribution and (**b**) transverse intensity profiles at successive propagation positions. The coordinates x and z denote the lateral position and propagation distance, respectively.

The calculated output-facet distribution is shown in Figure 3. After normalization to the central maximum, the outer–inner–central–inner–outer peak-intensity ratio is approximately 0.17:0.22:1:0.22:0.17. The central output therefore provides the dominant intensity maximum, with the inner-channel peaks exceeding those of the outer channels. These values characterize relative peak intensities rather than integrated optical power fractions. The latter additionally depend on the transverse intensity distribution over each output region, so the peak ratios are not assigned to channel power fractions or individual junction splitting ratios. In this study, "center-weighted" specifically describes the output-facet intensity distribution. The subsequent lens transformation and free-space propagation are

evaluated separately because they establish the directions and transverse dimensions of the illumination zones.

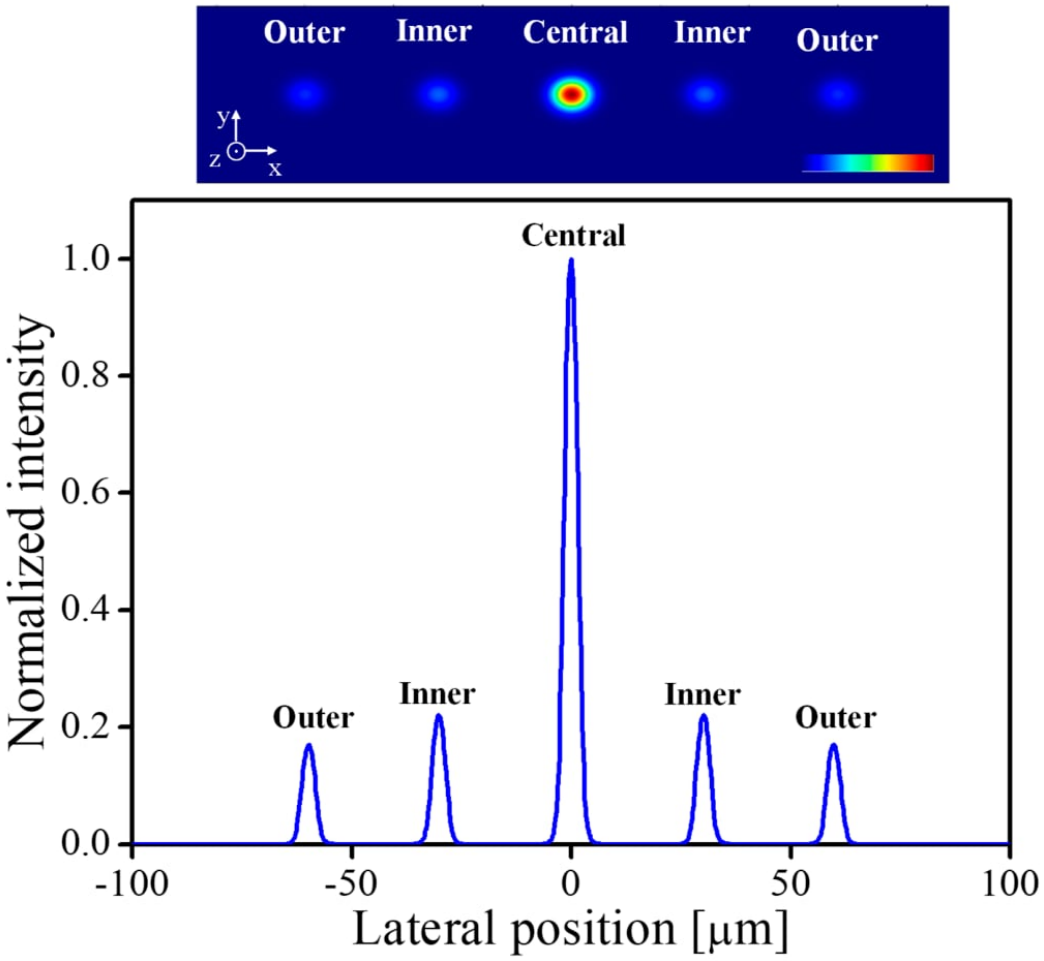

Figure 3. BPM-calculated near-field intensity distribution at the splitter output. Their peak intensities, normalized to the central maximum, are approximately 0.17, 0.22, 1, 0.22, and 0.17, respectively.

The device was fabricated using a silica PLC process. The laser diode, operating at $\lambda = 905$ nm, was pigtailed to a fiber operating in the single-mode regime at this wavelength. The fiber output end was secured in a quartz block, actively aligned for butt coupling to the waveguide input facet, and bonded in place. The fabricated splitter was integrated with a commercial aspheric collimating lens, C240TME-B supplied by Thorlabs, Inc. (Newton, NJ, USA), to form a packaged illuminator approximately 4.5 cm in length. The output facet was positioned near the front focal plane of the lens so that the five localized outputs acted as a common source array. The beam directions and propagation characteristics reported in this study refer to the assembled module, with the collimating lens maintained at its aligned position and orientation throughout the measurements. The central channel defines the nominal axial source position, while the two lateral pairs provide the displaced source positions for the off-axis beams. In the assembled configuration, guided-wave redistribution establishes the relative source excitation, and the common lens converts the output positions into distinct propagation directions. The experimental characterization establishes the multibeam formation and distance-dependent propagation characteristics of the assembled optical module. Measurements were performed on one assembled prototype. Free-space beam patterns were recorded at propagation distances of 1, 2, 3, 4, 6, and 8 m using the same module.

3. Experimental Results and Discussion

3.1. Near-Field Output Characteristics

Figure 4a shows the fabricated silica splitter, the near-field measurement arrangement, and the output-facet image. Five localized output spots were observed, with their arrangement consistent with the nominal 30 μm channel pitch. The measured normalized lateral intensity profile in Figure 4b exhibits a dominant central maximum accompanied by four weaker lateral peaks. The fabricated device therefore retains the intended center-weighted source characteristic and provides the five source positions required for the common-lens configuration. This measurement establishes the spatial output distribution before the field is transformed by the collimating optics.

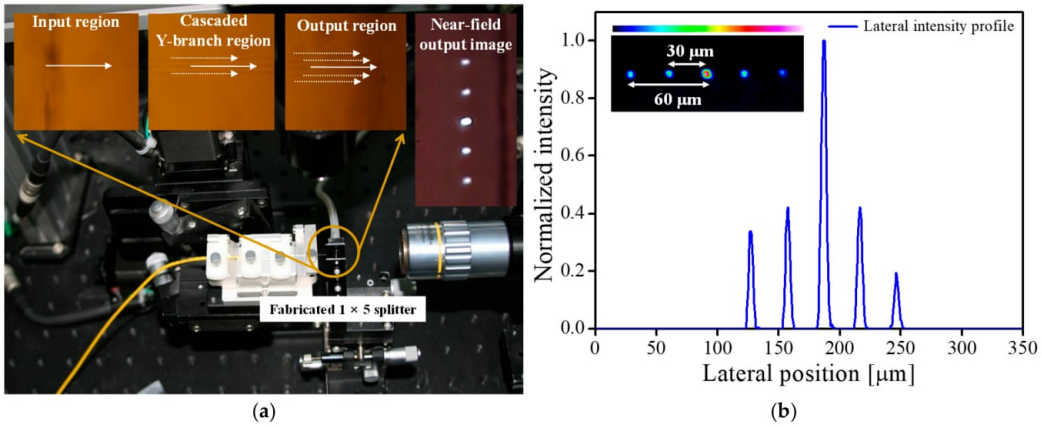

Figure 4. Near-field characterization of the fabricated silica waveguide splitter: (**a**) measurement arrangement, images of the device regions, and the output-facet image; (**b**) measured normalized lateral intensity profile, with an inset showing the five output spots. In (**a**), the solid white arrows indicate the dominant central beam, while the dashed white arrows indicate the weaker lateral beams.

The measured normalized peak-intensity ratio is 0.34:0.42:1.00:0.42:0.20 in the left-outer–left-inner–central–right-inner–right-outer order, as determined from the original measurement data. Compared with the BPM prediction of 0.17:0.22:1.00:0.22:0.17, the measured distribution retains the dominant central peak while exhibiting higher relative lateral peaks. The two inner channels have equal measured peak intensities, whereas the outer channels show a clear left–right asymmetry. Input-coupling conditions and variations in the realized branch geometry may contribute to these differences by altering field redistribution within the cascaded structure. Structural sensitivity has also been examined in nonuniform silica PLC splitter design [29]. These ratios characterize the local peak intensities at the output facet; channel-integrated powers additionally depend on the transverse field distributions.

Transmission was evaluated independently using a straight reference waveguide fabricated on the same wafer with the same length, core dimensions, and refractive-index contrast as the splitter. The measured transmission, defined as the straight-waveguide output power divided by the fiber output power measured before coupling, was 93.48%. This transmission corresponds to a loss of approximately 0.29 dB over the defined reference path. This value includes the combined effects of input coupling, propagation through the nonbranching waveguide, and the output interface between the two power-reference locations. It provides a baseline for a comparable straight guided path but does not include the cascaded junctions or the collimating lens. Accordingly, it is not assigned to the transmission efficiency of the five-channel splitter or the complete illuminator. Comparison with the insertion-loss and excess-loss results of other PLC splitters requires the respective measurement paths and reference definitions to be considered [27–29].

3.2. Beam Collimation and Collimated Beam Profiles

Figure 5 illustrates the assembled illuminator and the packaged module. The waveguide output facet was positioned near the front focal plane of the aspheric lens, allowing the five localized outputs to serve as a source array. Under the paraxial approximation, the lens converts lateral source displacement into beam-axis inclination through position-to-angle mapping [15–17]. The central output forms the axial beam, while the inner and outer outputs form two pairs of off-axis beams. The splitter and lens thus provide complementary functions: the branching network establishes the guided-wave source distribution, and the lens establishes the nominal free-space propagation directions.

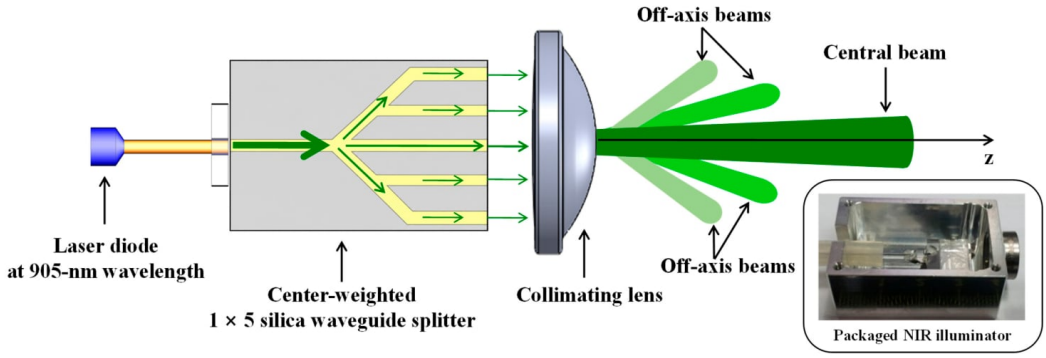

Figure 5. Configuration of the multibeam illuminator comprising the fiber-coupled laser diode, center-weighted 1 × 5 silica waveguide splitter, and aspheric collimating lens. The central output forms an axial beam, and the lateral outputs form two pairs of off-axis beams. The inset shows the packaged illuminator.

The effective focal length at $\lambda = 905$ nm was estimated as 8.04 mm by linear interpolation between the manufacturer-specified values of 8.018 mm at 830 nm and 8.057 mm at 980 nm. For a nominal adjacent-channel pitch of 30 μm, the corresponding inner- and outer-beam inclination magnitudes are approximately 0.214° and 0.428°, respectively. These values specify beam-axis directions rather than the angular spreading of the individual beams. For small angular offsets, the difference between adjacent beam-axis directions is approximately p/f. At propagation distances large compared with the dimensions of the module, the nominal adjacent-beam spacing is therefore

$$s(z) \approx \frac{z \cdot p}{f}, \quad (1)$$

Here, $s(z)$ is the center-to-center spacing between adjacent beams at the observation plane, z is the propagation distance from the collimating lens to that plane, p is the center-to-center pitch of the waveguide output channels, and f is the effective focal length. Equation (1) relates the source geometry to the separation of neighboring beam axes. At observation planes where individual peaks are resolved, the beam spacing is evaluated from the positions of adjacent maxima in the measured transverse intensity distribution. This center-to-center spacing is distinct from the individual beam diameter and the edge-to-edge gap. The central-beam diameter is evaluated separately in Section 3.3 to characterize transverse expansion.

Figure 6a,b present the calculated and measured beam patterns at propagation distances of 1, 2, 3, 4, 6, and 8 m. The calculated patterns were obtained by propagating Gaussian output fields through the collimating lens and free space under the paraxial approximation. They illustrate the development of an axial beam and two pairs of laterally displaced beams. The measured patterns likewise show increasing separation of the output lobes with propagation distance, demonstrating the conversion of the closely spaced waveguide outputs into distinct free-space illumination directions.

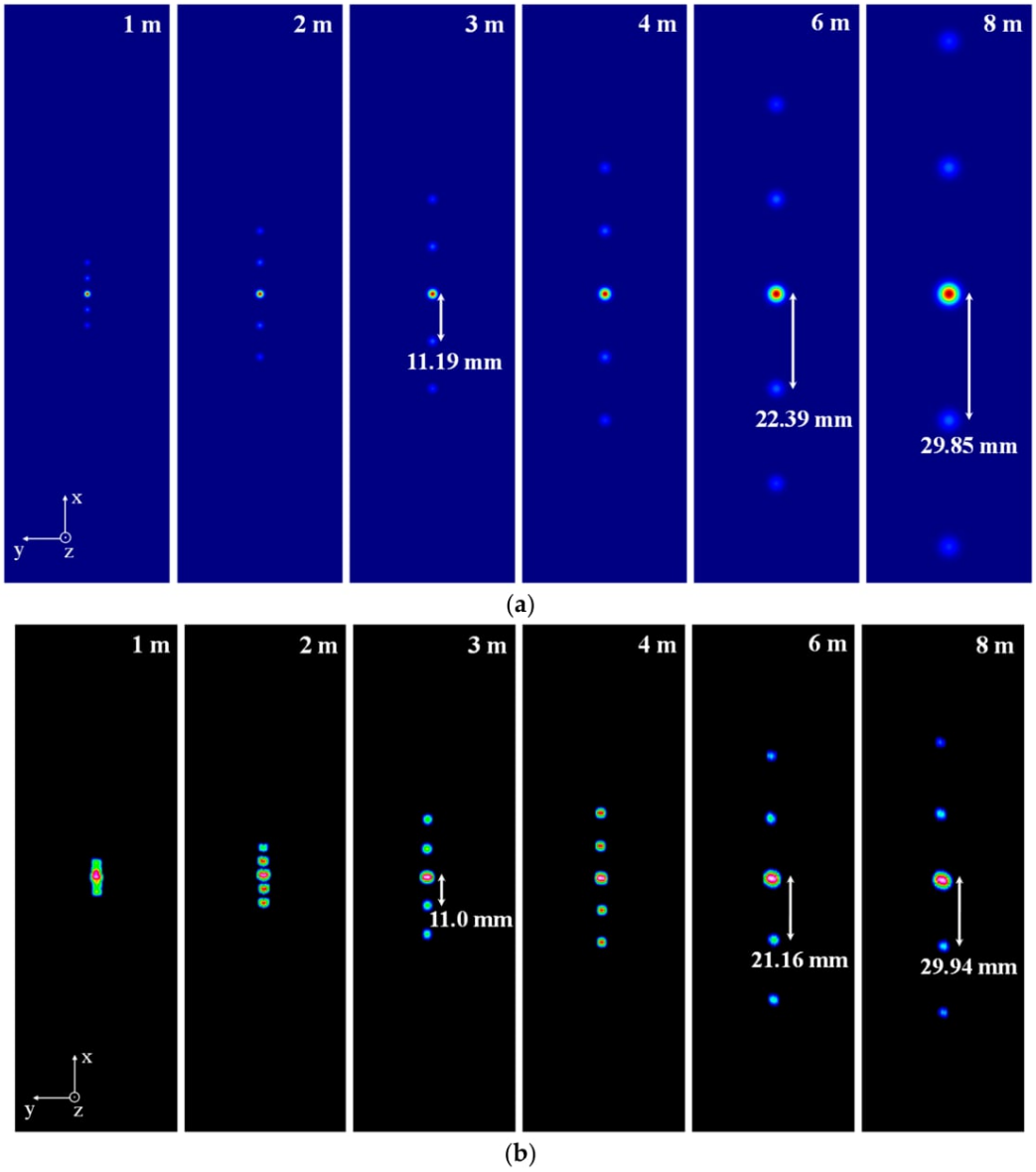

Figure 6. Free-space beam patterns of the multibeam illuminator at propagation distances of 1, 2, 3, 4, 6 and 8 m: (**a**) calculated patterns after the collimating lens and (**b**) measured patterns. The arrows indicate the center-to-center spacing between adjacent beams at 3, 6 and 8 m.

A geometrical separation criterion can be defined using the individual $1/e^2$ beam envelopes. For adjacent beams with center spacing $s(z)$ and radii $w_i(z)$ and $w_j(z)$, the edge-to-edge gap is

$$g(z) = s(z) - \left[w_i(z) + w_j(z)\right], \tag{2}$$

The envelopes are nonoverlapping when $g(z) \geq 0$. This criterion refers to the specified intensity boundaries rather than requiring the Gaussian tails to vanish. To estimate the separation boundary, identical Gaussian output modes with a waist radius $w_0 = 3\ \mu m$ were assumed at the waveguide output facet, positioned in the front focal plane of an ideal thin lens. Under this paraxial model, the adjacent-beam spacing is

$$s(z) = p\left|1 - \frac{z}{f}\right|, \tag{3}$$

and the common beam radius is

$$w(z) = \sqrt{w_0^2\left(1 - \frac{z}{f}\right)^2 + \left(\frac{\lambda f}{\pi w_0}\right)^2}, \quad (4)$$

where z is measured from the lens. For identical beam radii, the separation boundary satisfies

$$s(z) = 2w(z), \quad (5)$$

Using $\lambda = 905$ nm, $f = 8.04$ mm, and $p = 30$ µm, this condition gives a separation boundary approximately 0.43 m behind the lens. At 1 m, the calculated center spacing and beam diameter are approximately 3.70 and 1.71 mm, respectively, giving an edge-to-edge gap of approximately 1.99 mm. The adjacent pairs determine the separation boundary for the complete array because they have the smallest angular separation. This result is an analytical estimate under the stated mode-size and alignment assumptions.

Using $p = 30$ µm and $f = 8.04$ mm, Equation (1) predicts adjacent-beam spacings of approximately 11.19, 22.39, and 29.85 mm at 3, 6, and 8 m, respectively. The corresponding measured spacings were 11.0, 21.16, and 29.94 mm. The measured spacings differ from the nominal predictions by −0.19, −1.23, and +0.09 mm, respectively. Relative to the nominal predictions, the differences are approximately −1.7%, −5.5%, and +0.3%. The measurements reproduce the expected increase in spacing with distance, with the largest departure from the nominal geometry occurring at 6 m. A measurement uncertainty budget and alignment sensitivity analysis were not established, so these differences are not assigned to a specific cause. The comparison supports the source-position-to-angle interpretation at the level of the observed propagation geometry rather than a calibrated determination of beam-axis accuracy. The increasing spacing is a consequence of the fixed angular differences between the beams and does not require active steering. The source array and common lens therefore generate a static set of illumination directions whose lateral separation increases with observation distance. Whether the individual illumination zones remain distinct additionally depends on the expansion of their transverse envelopes.

3.3. Multi-Beam Propagation Characteristics

Figure 7 presents the central-beam diameter measured at propagation distances of 1, 2, 3, 4, 6, and 8 m. The diameter is defined as the full transverse width at $1/e^2$ of the central beam's own peak intensity, corresponding to approximately 13.5% of the peak. This definition follows the conventional beam-diameter criterion for a Gaussian intensity distribution. The central-beam diameter increased from 1.68 mm at 1 m to 6.85 mm at 8 m, characterizing its transverse expansion over the measured range.

The net expansion over the measured interval was expressed as an effective full angle:

$$\alpha_{eff.} = 2\tan^{-1}\left[\frac{D(z_2) - D(z_1)}{2(z_2 - z_1)}\right], \quad (6)$$

Here, $\alpha_{eff.}$ is the effective full-angle spreading, and $D(z_1)$ and $D(z_2)$ are the measured central-beam $1/e^2$ diameters at $z_1 = 1$ m and $z_2 = 8$ m, respectively. The diameters and propagation distances are expressed in consistent units. Using the measured diameters of 1.68 and 6.85 mm gives an effective full-angle spreading of approximately 0.042°. This value characterizes the net transverse expansion over the 1–8 m interval and is distinct from the beam-axis inclination defined in Section 3.2 and from an independently determined asymptotic divergence angle.

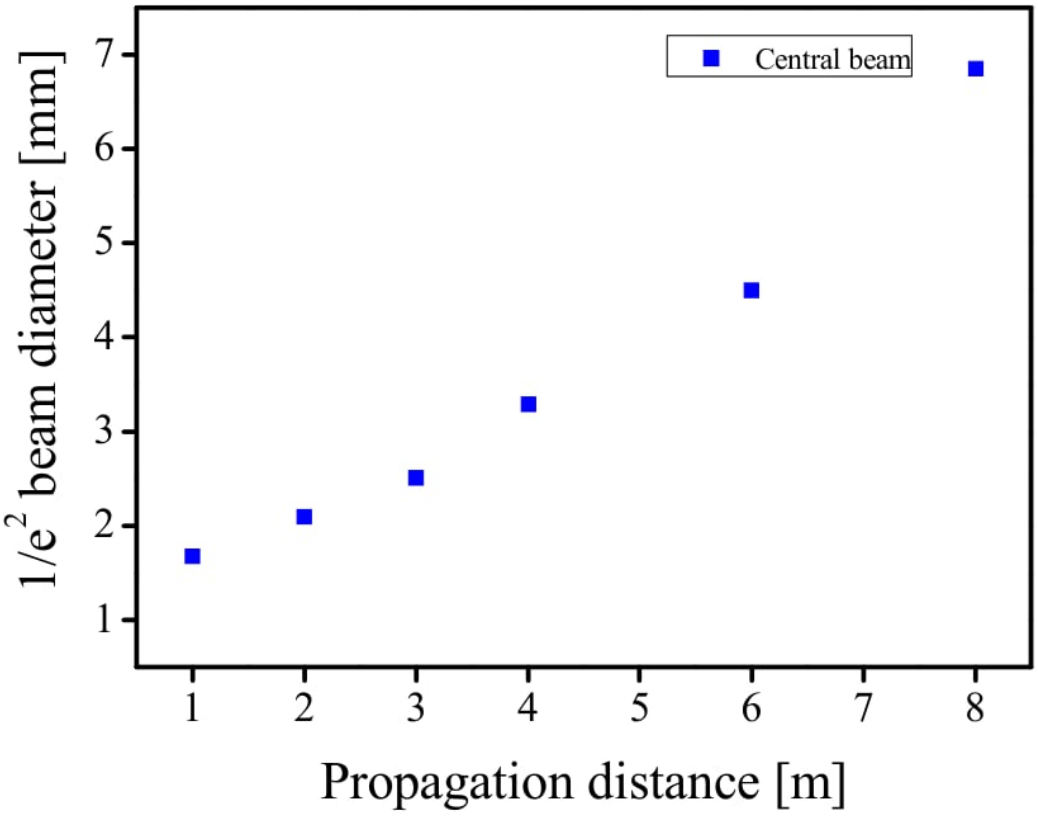

Figure 7. Measured central-beam $1/e^2$ diameter as a function of propagation distance.

Previous studies have demonstrated asymmetric and nonuniform power division in silica 1 × 5 splitters [28,29], arbitrary-ratio multichannel splitting [24], and polarization-insensitive 1 × 5 splitting [25]. Metasurface and meta-fiber devices combine beam splitting with control of the free-space output distribution [13,14], while lens-based position-to-angle conversion has been demonstrated in scan-less sensing and integrated beam-steering systems [15–17]. In the present configuration, a fabricated silica splitter and a common aspheric lens generate five fixed beam directions from a single input without wavelength demultiplexing or active beam steering. Near-field measurements confirm five localized outputs with a dominant central intensity peak. Free-space measurements over 1–8 m characterize the resulting axial beam and two pairs of off-axis beams. The measured adjacent-beam spacings increase with propagation distance, consistent with the nominal output pitch and lens focal length, while the central-beam diameter measurements quantify transverse expansion over the same range. These measurements characterize both beam-axis separation and beam width, which together determine the spatial separation of the illumination zones.

The module generates one axial beam and four fixed off-axis beams from a single fiber-coupled laser source. The splitter determines the output-facet intensity distribution, while the output-channel pitch and lens focal length determine the nominal angular separation between adjacent beams. Beam diameters measured at the observation planes provide the corresponding transverse dimensions of the illumination regions. The term "center-weighted" describes the normalized peak intensities at the waveguide output facet and does not specify integrated channel powers or absolute target irradiance. By characterizing the output-facet intensity distribution, free-space beam spacing, and central-beam expansion within the same assembled module, this study provides experimental data for evaluating a passive multibeam source in optical sensing systems that require discrete illumination along fixed directions.

4. Conclusions

A compact multibeam NIR illuminator was fabricated by integrating a center-weighted 1 × 5 silica waveguide splitter, a fiber-coupled laser diode, and an aspheric collimating lens. The assembled module, approximately 4.5 cm in length, generates one axial beam and two pairs of fixed off-axis beams. Near-field measurements confirmed five spatially separated outputs with a dominant central intensity peak. The measured adjacent-beam spacings were 11.0, 21.16, and 29.94 mm at propagation distances of 3, 6, and 8 m, respectively, consistent with the distance-dependent separation predicted from the output-channel pitch and lens focal length. The central-beam diameter increased from 1.68 to 6.85 mm over 1–8 m, corresponding to an effective full-angle spreading of approximately 0.042°. These measurements characterize the output intensity distribution, beam separation, and central-beam expansion of the assembled module, demonstrating a compact passive configuration for multibeam NIR illumination without active beam steering.

Author Contributions: Conceptualization, H.-S.L. and S.-S.L.; methodology, H.-S.L.; validation, H.-S.L. and S.-S.L.; formal analysis, H.-S.L. and S.-S.L.; investigation, H.-S.L.; data curation, H.-S.L.; writing—original draft preparation, H.-S.L.; writing—review and editing, S.-S.L.; supervision, S.-S.L. All authors have read and agreed to the published version of the manuscript.

Funding: This research was supported by the Basic Science Research Program through the National Research Foundation of Korea (NRF), funded by the Ministry of Education (No. RS-2018-NR031063), and a research grant of Kwangwoon University in 2026.

Institutional Review Board Statement: Not applicable.

Informed Consent Statement: Not applicable.

Data Availability Statement: Data are contained within the article.

Acknowledgments: The work reported in this paper was conducted during the sabbatical year of Kwangwoon University in 2026.

Conflicts of Interest: The authors declare no conflicts of interest.

References

1. Foix, S.; Alenyà, G.; Torras, C. Lock-in time-of-flight (ToF) cameras: A survey. *IEEE Sens. J.* **2011**, *11*, 1917–1926. [CrossRef]
2. Dai, Z.; Wolf, A.; Ley, P.-P.; Glück, T.; Sundermeier, M.C.; Lachmayer, R. Requirements for automotive LiDAR systems. *Sensors* **2022**, *22*, 7532. [CrossRef] [PubMed]
3. Kim, I.; Martins, R.J.; Jang, J.; Badloe, T.; Khadir, S.; Jung, H.-Y.; Kim, H.; Kim, J.; Genevet, P.; Rho, J. Nanophotonics for light detection and ranging technology. *Nat. Nanotechnol.* **2021**, *16*, 508–524. [CrossRef]
4. Li, N.; Ho, C.P.; Xue, J.; Lim, L.W.; Chen, G.; Fu, Y.H.; Lee, L.Y.T. A progress review on solid-state LiDAR and nanophotonics-based LiDAR sensors. *Laser Photonics Rev.* **2022**, *16*, 2100511. [CrossRef]
5. Lutz, Y.; Poyet, J.M. Laser diode stack beam shaping for efficient and compact long-range laser illuminator design. *Opt. Laser Technol.* **2014**, *57*, 90–95. [CrossRef]
6. Han, J.; Zhang, J.; Shan, X.; Zhang, Y.; Peng, H.; Qin, L.; Wang, L. Beam homogenization structure for a laser illuminator design based on diode laser beam combining technology. *Chin. Opt. Lett.* **2023**, *21*, 031405. [CrossRef]
7. Chen, B.; Claus, D.; Russ, D.; Nizami, M.R. Generation of a high-resolution 3D-printed freeform collimator for VCSEL-based 3D-depth sensing. *Opt. Lett.* **2020**, *45*, 5583–5586. [CrossRef] [PubMed]
8. Hirose, K.; Kamei, H.; Sugiyama, T.; Kurosaka, Y. 200 × 200 μm^2 structured light source. *Opt. Express* **2020**, *28*, 37307–37321. [CrossRef] [PubMed]
9. Hsu, W.-C.; Chang, C.-H.; Hong, Y.-H.; Kuo, H.-C.; Huang, Y.-W. Metasurface- and PCSEL-based structured light for monocular depth perception and facial recognition. *Nano Lett.* **2024**, *24*, 1808–1815. [CrossRef] [PubMed]
10. Madrid-Sánchez, A.; Duerr, F.; Nie, Y.; Thienpont, H.; Ottevaere, H. Freeform optics design method for illumination and laser beam shaping enabled by least squares and surface optimization. *Optik* **2022**, *269*, 169941. [CrossRef]
11. Yu, N.; Capasso, F. Flat optics with designer metasurfaces. *Nat. Mater.* **2014**, *13*, 139–150. [CrossRef] [PubMed]

12. Kim, G.; Kim, Y.; Yun, J.; Moon, S.-W.; Kim, S.; Kim, J.; Park, J.; Badloe, T.; Kim, I.; Rho, J. Metasurface-driven full-space structured light for three-dimensional imaging. *Nat. Commun.* **2022**, *13*, 5920. [CrossRef] [PubMed]
13. Tian, T.; Liao, Y.; Feng, X.; Cui, K.; Liu, F.; Zhang, W.; Huang, Y. Metasurface-based free-space multi-port beam splitter with arbitrary power ratio. *Adv. Opt. Mater.* **2023**, *11*, 2300664. [CrossRef]
14. He, N.; Guo, T.; Jin, Y.; He, S. All-in-one collimating splitter based on a meta-fiber platform. *Appl. Sci.* **2023**, *13*, 4603. [CrossRef]
15. Yao, X.S.; Liu, X.; Hao, P. Scan-less 3D optical sensing/Lidar scheme enabled by wavelength division demultiplexing and position-to-angle conversion of a lens. *Opt. Express* **2020**, *28*, 35884–35897. [CrossRef] [PubMed]
16. Hu, L.; Xue, R.; Cao, X.; Liu, J.; Wu, K.; Wu, G.; Chen, J. Free-space point-to-multiplepoint optical frequency transfer with lens assisted integrated beam steering. *IEEE Trans. Instrum. Meas.* **2022**, *71*, 7005610. [CrossRef]
17. Zhang, X.; Kwon, K.; Henriksson, J.; Luo, J.; Wu, M.C. A large-scale microelectromechanical-systems-based silicon photonics LiDAR. *Nature* **2022**, *603*, 253–258. [CrossRef] [PubMed]
18. Zhang, Y.; Yang, S.; Lim, A.E.-J.; Lo, G.-Q.; Galland, C.; Baehr-Jones, T.; Hochberg, M. A compact and low loss Y-junction for submicron silicon waveguide. *Opt. Express* **2013**, *21*, 1310–1316. [CrossRef] [PubMed]
19. Sun, C.; Zhao, J.; Wang, Z.; Du, L.; Huang, W. Broadband and high uniformity Y junction optical beam splitter with multimode tapered branch. *Optik* **2019**, *180*, 866–872. [CrossRef]
20. Ozcan, C.; Mojahedi, M.; Aitchison, J.S. Short, broadband, and polarization-insensitive adiabatic Y-junction power splitters. *Opt. Lett.* **2023**, *48*, 4901–4904. [CrossRef] [PubMed]
21. Chung, H.-C.; Wang, T.-C.; Hung, Y.-J.; Tseng, S.-Y. Robust silicon arbitrary ratio power splitters using shortcuts to adiabaticity. *Opt. Express* **2020**, *28*, 10350–10362. [CrossRef] [PubMed]
22. Xu, K.; Liu, L.; Wen, X.; Sun, W.; Zhang, N.; Yi, N.; Sun, S.; Xiao, S.; Song, Q. Integrated photonic power divider with arbitrary power ratios. *Opt. Lett.* **2017**, *42*, 855–858. [CrossRef] [PubMed]
23. Franz, Y.; Guasoni, M. Compact 1 × N power splitters with arbitrary power ratio for integrated multimode photonics. *J. Opt.* **2021**, *23*, 095802. [CrossRef]
24. Haines, J.; Vitali, V.; Bottrill, K.; Naik, P.U.; Gandolfi, M.; De Angelis, C.; Franz, Y.; Lacava, C.; Petropoulos, P.; Guasoni, M. Fabrication of 1 × N integrated power splitters with arbitrary power ratio for single and multimode photonics. *Nanophotonics* **2024**, *13*, 339–348. [CrossRef] [PubMed]
25. Haines, J.; Naik, P.U.; Kanagaraj, N.; Petropoulos, P.; Guasoni, M. Compact integrated 1 × N polarization-insensitive optical power splitters via waveguide arrays. *Opt. Lett.* **2025**, *50*, 5278–5281. [CrossRef] [PubMed]
26. Liu, Y.; Kang, Z.; Xu, H.; Zhong, G.; Zhang, R.; Fu, C.; Tian, Y. Inverse design of multi-port power splitter with arbitrary ratio based on shape optimization. *Nanomaterials* **2025**, *15*, 393. [CrossRef] [PubMed]
27. Wang, H.-T.; Chen, C.-F.; Chi, S. A numerical solution for broadband PLC splitter with variable splitting ratio based on asymmetric three waveguide structures. *Appl. Sci.* **2019**, *9*, 1892. [CrossRef]
28. Wang, L.L.; An, J.M.; Zhang, J.S.; Wu, Y.D.; Li, J.G.; Yin, X.J.; Wang, H.J.; Wang, Y.; Zhong, F.; Zha, Q.; et al. Design and fabrication of a low-loss and asymmetric 1 × 5 arbitrary optical power splitter. *Appl. Opt.* **2016**, *55*, 8601–8605. [CrossRef] [PubMed]
29. Wang, J.; Zheng, Y.; Zou, X.; Zhao, Y.; Liu, J.; Jiang, X.; Duan, J. Design and optimization of non-uniform 1 × 5 PLC splitter using orthogonal experimental method. *Opt. Laser Technol.* **2024**, *168*, 109955. [CrossRef]
30. Idris, N.A.; Sorimoto, K.; Tsuda, H. A novel silica waveguide lens for free-space optical cross connects. *IEICE Electron. Express* **2012**, *9*, 998–1004. [CrossRef]

Disclaimer/Publisher's Note: The statements, opinions and data contained in all publications are solely those of the individual author(s) and contributor(s) and not of MDPI and/or the editor(s). MDPI and/or the editor(s) disclaim responsibility for any injury to people or property resulting from any ideas, methods, instructions or products referred to in the content.